INORGANIC CHEMISTRY FRONTIERS

CHINESE CHEMICAL SOCIETY

ROYAL SOCIETY OF CHEMISTRY

RESEARCH ARTICLE

View Article Online
View Journal | View Issue

Cite this: *Inorg. Chem. Front.*, 2023, **10**, 6566

Fabrication of ultrathin two-dimensional MOF nanosheets with cage-like cavities showing excellent adsorption for lead(II)†

Hongwei Sun,[a] Ke-Zhong Wang,[a] Meng-Ru Yao,[a] Cai-Xia Yu,*[a] Yue-Hai Song,[a] Jing Ding,[a] Yan-Li Zhou,[a] Dong Liu*[b] and Lei-Lei Liu*[a]

In this work, we present a top-down method for the preparation of 2D MOF nanosheets with cavity structures. The pro-ligand 25,26,27,28-tetrakis[(carboxyl)methoxy]calix[4]arene was elaborately selected, and a layered MOF with cavity structures was constructed. The large molecular skeleton and cup-shaped feature of the calix[4]arene caused large layer separations and weak interlayer interactions among the 2D layers, which enabled the layered MOF to be readily delaminated into ultrathin 2D MOF nanosheets. Owing to the cup-shaped feature of the calix[4]arene, there are permanent cage-like cavities loaded on the as-prepared MOF nanosheets. By decorating oxygen-containing functional groups (carboxyl and ether groups) in the cage-like cavities, the resultant **Cu-MOF** nanosheets showed excellent adsorption performance for Pb^{2+}. The intimate contact and sufficient interactions on the exposed surface areas of **Cu-MOF** nanosheet resulted in ultrahigh adsorption selectivity and anti-interference ability for Pb^{2+}, together with an outstanding Pb^{2+} uptake capacity of 738.65 mg g^{-1}, which were obviously better than those of its 3D precursor. The possible adsorption mechanism was systematically investigated by the investigations of zeta potential, FT-IR, XPS, and DFT calculations. This study opens the door to achieving ultrathin MOF nanosheets with cavity structures, which would well expand the applications of MOF nanosheets.

Received 16th August 2023,
Accepted 18th September 2023

DOI: 10.1039/d3qi01619f

rsc.li/frontiers-inorganic

Introduction

Lead (Pb), one of the most pervasive and dangerous industrial pollutants, can accumulate over time in the human body and cause serious damage to the brain, liver, kidneys, reproductive system, and immune system.[1] The efficient and selective removal of Pb^{2+} from aqueous solutions, especially with outstanding anti-interference capability, remains a great challenge.[2–4] Owing to the adjustable composition, ordered pore structure, and large specific surface area of metal–organic frameworks (MOFs), the new type of crystalline porous materials have been increasingly applied in the field of adsorption.[5–8] By ligand pre-design or MOF post-functionalization, different functional groups can be purposely introduced into the pores or cavities of the frameworks,[9] creating more active sites for the capture of target pollutants.[10–13] In this process, functional groups worked as catchers for pollutants, and the pores/cavities acted as containers for stabilizing the adsorbed pollutants to avoid desorption.[14–16] MOF materials have achieved excellent performance in pollutant removal, especially in the improvement of the selectivity by modifying the adsorption sites,[17–20] while the difficulty and limited accessibility to the active sites buried in the framework of bulky MOFs made a significant discount on their adsorption performances, including adsorption selectivity and uptake capacities.[21]

The abovementioned drawbacks may be solved by two-dimensional (2D) MOF nanosheets, highly open structures with sufficiently exposed surfaces and accessible active sites.[22–26] The 2D MOF nanosheets hold the structural characteristics of both bulky MOFs and 2D materials, such as versatile compositions and functions, exposed surface area, innumerable accessible surface-active sites, and nanoscale thickness, which were facile for the interaction with substrate molecules, affording improved performance in catalysis, sensing, separation, *etc.*[27–32] The significance of the synthesis of 2D MOF nanosheets was greatly highlighted by these attractive

---

[a] *School of Environmental and Material Engineering, Yantai University, Yantai 264005, P. R. China. E-mail: liuleileimail@163.com*

[b] *Jiangsu Key Laboratory for Chemistry of Low-Dimensional Materials, School of Chemistry and Chemical Engineering, Huaiyin Normal University, Huaian 223300, P. R. China. E-mail: dongliu@hytc.edu.cn*

† Electronic supplementary information (ESI) available: Materials and physical measurements, X-ray data collection and structure determination, adsorption experiments, calculation methods, PXRD patterns, TGA curves, zeta potential, XPS, additional schemes, figures, tables and X-ray crystallographic. CCDC 2206848. For ESI and crystallographic data in CIF or other electronic format see DOI: **https://doi.org/10.1039/d3qi01619f**

properties and applications.[33–35] However, few studies on pollutant capture by 2D MOF nanosheets have been reported thus far.[36] The loss of pore structures for the exfoliated 2D MOF nanosheets may be the key factor. The incorporation of pores or cavity structures into the open structure of 2D MOF nanosheets can be an efficient strategy to expand their applications in adsorption, which was expected to acquire highly selective and efficient adsorption performance.[22]

To obtain the 2D MOF nanosheets with pores or cavity structures, a ligand containing cavity structures is highly desirable, and the as-constructed 2D MOF nanosheets could not only be modified with predesigned functional groups but also hold cavity structures that are conducive to adsorption. Thus, the ligand design is of great significance for the synthesis of functionalized 2D MOF nanosheets. Calix[*n*]arenes (n = 4, 6, and 8) are a class of well-known macrocycles with a special cup-shaped cavity structure,[37] which have been used as building blocks for the construction of porous MOFs.[38–40] In view of the large molecular skeleton and cup-shaped feature of the calix[*n*]arene, the as-synthesized bulk MOFs tend to form layered structures with large layer separations and weak interlayer interactions, which would be facile for its exfoliation.[41] Owing to the cup-shaped feature of the calix[4]arene, there are permanent cage-like cavities loaded on the as-exfoliated MOF nanosheets. Moreover, the structural characteristics of the convenient modification for both the lower and upper rims of the calix[*n*]arene could endow the 2D MOF nanosheets with specific adsorption sites.[42]

Inspired by the unique structure with predesigned adsorption sites and cavities for the calix[*n*]arene-based MOF nanosheets, a calix[4]arene macrocycle was considered to be incorporated into the backbones of MOF nanosheets. Besides, the borderline acid of Pb^{2+} was likely to bind to the oxygen-containing functional groups, according to the hard–soft acid–base (HSAB) theory.[43] Thus, the pro-ligand 25,26,27,28-tetrakis[(carboxyl)methoxy]calix[4]arene (H_4L; Scheme S1†) locked in the cone conformation was elaborately selected for the construction of 2D MOF nanosheets. In the design, there are four carboxyl groups decorated on the lower rims of H_4L, some of which can coordinate with metal ions for MOF construction, and the left ones can serve as catchers for Pb^{2+}; there is no functional group decorated on the upper rims of H_4L, which would be facile for the formation of the layered structure (Scheme 1). Herein, a layered MOF, $\{[Cu_{1.5}(HL)(H_2O)_3]\cdot H_2O\}_n$ (**Cu-MOF**), was synthesized by the solvothermal reaction of $CuCl_2\cdot 2H_2O$ with the pro-ligand H_4L, which can be readily delaminated into 2D MOF nanosheets *via* a simple ultrasound method (Scheme 1). The extensively accessible and uncoordinated oxygen-containing functional groups (carboxyl and ether groups) in the cage-like cavities acted as adsorption sites, and the cavities loaded on MOF nanosheets served as pollutant containers. The intimate contact and sufficient interactions with Pb^{2+} on the exposed surface areas of MOF nanosheets not only achieved highly efficient capture, greatly enhancing Pb^{2+} uptake capacity (738.65 mg g^{-1}), but also resulted in ultra-high adsorption selectivity and anti-interference ability.

Results and discussion

Characterization of Cu-MOFs

Cu-MOFs crystallized in a monoclinic space group *C*2/*c*. Two $Cu(H_2O)$ subunits are linked by four carboxylate groups, affording a $[Cu_2(HL)_4(H_2O)_2]$ secondary building unit (Fig. 1a). These secondary building units are interconnected by their equivalent ones to construct a 2D structure (Fig. 1b). Notably, the unique cup-shaped feature and large molecular skeleton of the calix[4]arene enabled the as-constructed 2D layers to be loosely packed, yielding a 3D motif with a layered stacking structure (Fig. 1e), which was confirmed by scanning electron microscopy (SEM; Fig. 2b). Moreover, the view of the 3D structure presented a large layer spacing between the layers in **Cu-**

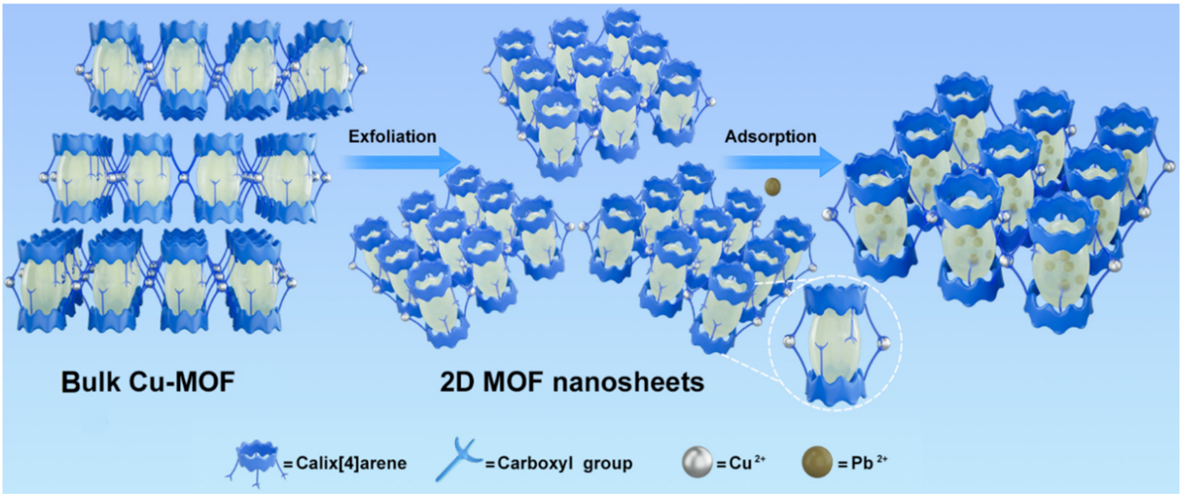

Scheme 1 Schematic illustration of the construction of 2D MOF nanosheets with cavity structures for pollutant removal.

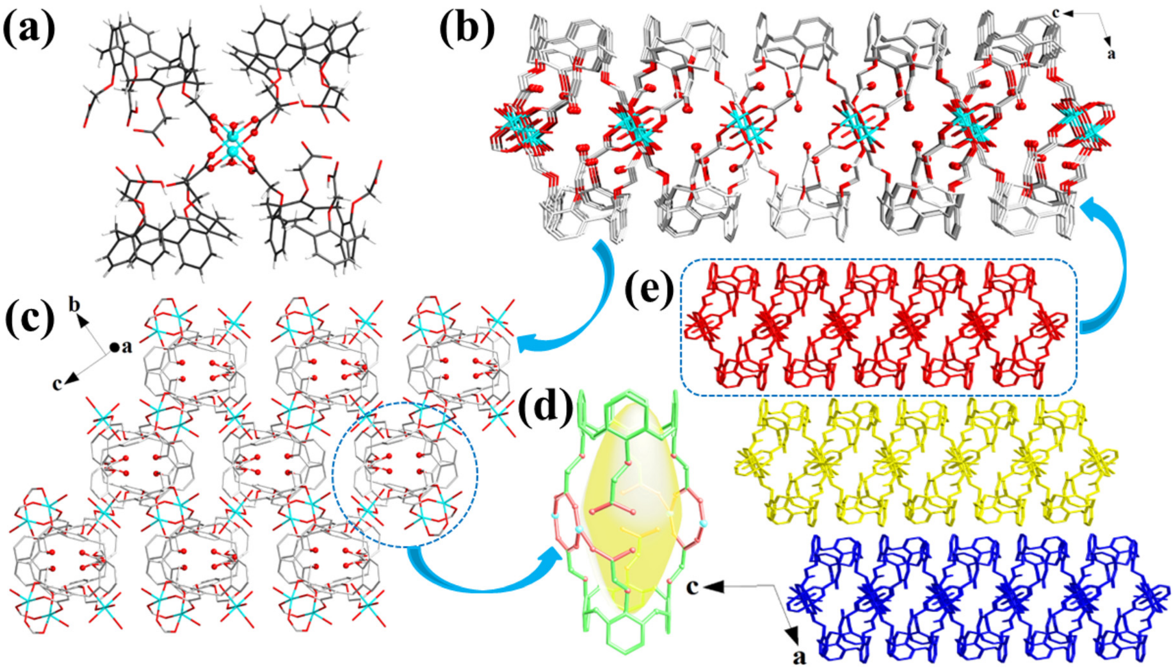

Fig. 1 (a) View of the $[Cu_2(HL)_4(H_2O)_2]$ secondary building unit in **Cu-MOFs**. Color codes: cyan, Cu; red, O; gray, C; light gray, H. (b and c) View of the 2D structures in **Cu-MOFs**. (d) Cage-like cavity in **Cu-MOFs**. (e) 3D motif in **Cu-MOFs**.

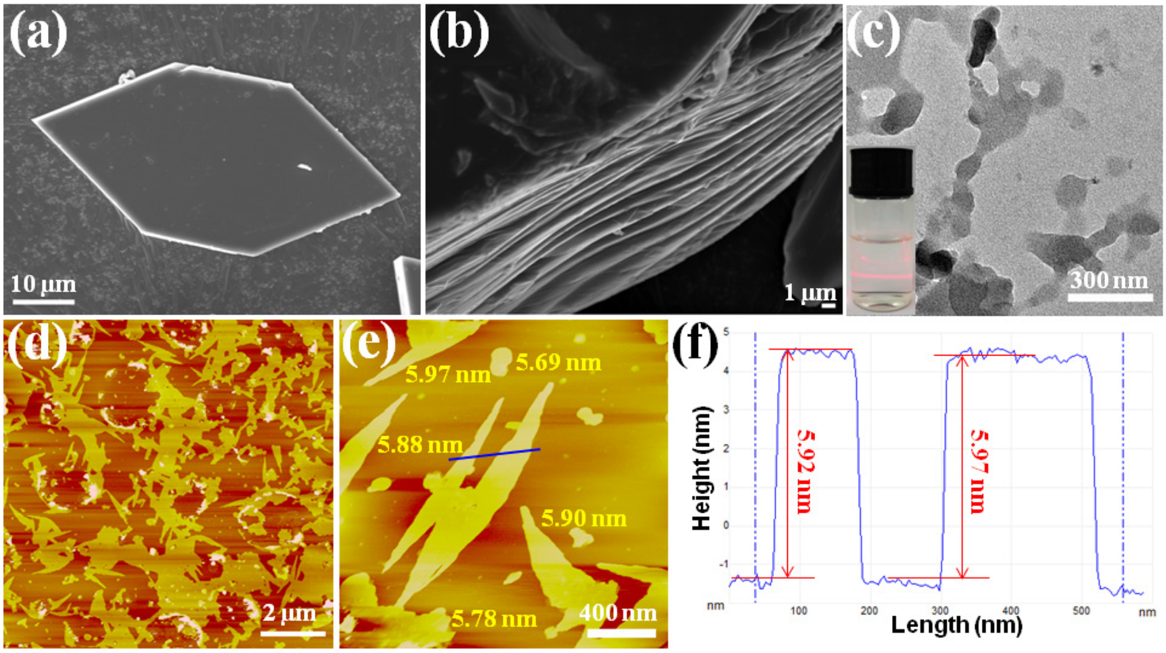

Fig. 2 (a) SEM image of the hexagonal **Cu-MOF**. (b) SEM image of the cross-section of the **Cu-MOF**. (c) TEM image of **Cu-MOF** nanosheets; inset: photograph of the Tyndall effect of **Cu-MOF** nanosheet suspension. (d and e) AFM images of **Cu-MOF** nanosheets. (f) Height profile, color-coded blue, is measured along the corresponding track shown in (e).

MOFs (Fig. 1e), indicating a weak interlayer interaction in the layers. The large layer spacing would be facile for the insertion of solvent molecules into the interlayers and further destroy the interlayer interactions in bulk MOFs, causing the exfoliation more convenient. Interestingly, the cage-like cavities were formed in the 2D layers of **Cu-MOFs** (Fig. 1d), which were decorated with uncoordinated carboxyl (–COOH) and ether (–O–) groups in them; these uncoordinated oxygen-containing groups can be utilized for Pb^{2+} capture and the cavities acted as containers to accommodate the adsorbed Pb^{2+}. Based on these observations, the calix[4]arene is an ideal building block for the construction of 2D MOF nanosheets with cage-like cavities, which not only facilitate MOF exfoliation and pollutant capture but also prevent the adsorbate from desorption. The water stability of **Cu-MOFs** was verified by powder X-ray diffraction (PXRD) measurements, and the PXRD patterns kept almost the same as those of the experimental sample (Fig. S1†) after soaking in a range of solutions (pH 3.0–11.0) for 24 h.

Exfoliation of Cu-MOF nanosheets

Top-down exfoliation is regarded as an efficient method to prepare MOF nanosheets, by using an external force to disintegrate the interlayer interaction of layered MOFs. The unique layered structure provides convenience for **Cu-MOFs** to achieve ultrathin nanosheets, and a simple and convenient ultrasound-induced liquid phase exfoliation method was selected. The hexagonal **Cu-MOF** (Fig. 2a) was dispersed in a MeOH/isopropanol (4 : 1, V/V) solution, under continuous sonication in an ice-water bath for 6 h. After that, the content of Cu^{2+} in the solution was analyzed, and no Cu^{2+} was detected. The result indicated that there was no **Cu-MOF** degradation in the exfoliation. The obtained milky colloidal suspension with significant Tyndall effects (inset in Fig. 2c) is indicative of the achievement of the ultrathin nanosheets. The detailed morphology of the nanosheets was examined by transmission electron microscopy (TEM) and atomic force microscopy (AFM). The TEM image (Fig. 2c), which displayed a flaky sheet-like morphology, further confirmed the achievement of the ultrathin MOF nanosheets. The AFM images displayed in Fig. 2d–2e show flat layers with lateral dimensions in the micrometer range, and they were measured to be 5.8 ± 0.1 nm in height (Fig. 2f). The single layer thickness of the 2D MOF nanosheets was calculated to be 1.88 nm based on single-crystal X-ray structure determination, implying that there are approximately 3 layers in total for the obtained 2D MOF nanosheets.

After exfoliation, the structural integrity of the 2D MOF nanosheets remained as anticipated, which was confirmed by a series of measurements. As shown in Fig. S2,† the PXRD patterns of the derived 2D nanosheets matched those of the bulk MOF, and the exfoliation into the extremely thin nanosheets is the reason for the decrease in the strength of these distinctive peaks.[44,45] Fourier transform infrared (FT-IR) spectra (Fig. S3†) and thermogravimetric analysis (TGA) curves (Fig. S4†) provided additional evidence for the structural integrity of the nanosheets. The peaks in the FT-IR spectrum of the MOF nanosheets were in good agreement with those of the bulk **Cu-MOF** samples (Fig. S3†), and no obvious difference was observed in the TGA curves between the two samples (Fig. S4†). The synthesized 2D MOF nanosheet not only retained the structural integrity but also held high water stability. After soaking in an aqueous solution (pH 2.0–7.0) for 12 h, it could keep the same patterns as those of the original sample (Fig. S5†). The aforementioned findings demonstrated that the few-layer MOF nanosheets were successfully synthesized with high structural integrity and water stability *via* a straightforward ultrasonic approach. In addition, the unique backbone of the calix[4]arene can be responsible for the facile exfoliation and high structural integrity of the MOF nanosheets.

Pb^{2+} adsorption studies

In view of the unique structure and fair water stability of the **Cu-MOF** nanosheets, the Pb^{2+} adsorption performance was studied. First, the effect of solution pH was investigated, since the pH value strongly affects the adsorption performance of heavy metal ions. As shown in Fig. 3, the Pb^{2+} removal rate was low at pH 3.0, and it presented a drastic increase with the increase in pH, reaching the highest signal at pH 7.0. When the pH exceeds 7.0, Pb^{2+} hydroxide precipitation may occur. As a result, the optimal pH of 7.0 was chosen for the subsequent sorption experiments. Second, the effect of adsorbent dosage on Pb^{2+} adsorption was investigated, which is essential to attain high removal efficiency. The Pb^{2+} removal ratios were assessed by adding the adsorbents at different dosages (40, 60, 100, 140, 180, and 220 mg L^{-1}) into a certain Pb^{2+} solution (10 ppm). As shown in Fig. S6,† the Pb^{2+} removal rate increased with the growing adsorbent dosage, and it went up to 98.11% at 100 mg L^{-1}. The further increase in adsorbent dosages to 140, 180, and 220 mg L^{-1} resulted in almost equal removal rates to that of 100 mg L^{-1}. In consideration of the removal performances and adsorption cost, the adsorbent dosage of 100 mg L^{-1} (5 mg/50 mL) was selected for the following investigations.

The maximum uptake capacity, a crucial factor in determining an adsorbent's effectiveness and applicability in a wastewater disposal system, was evaluated by the investigation of adsorption isotherms. The value of q_e (equilibrium adsorption capacity), as presented in Fig. 4, increased with the increase in Pb^{2+} concentrations until it eventually reached its maximum value of 738.65 mg g^{-1}. Fig. S7† displays the plots for the relevant data fitted by the Langmuir and Freundlich models. According to the correlation coefficients shown in Table S1,† the Langmuir model (R^2 = 0.999) better fits the data, demonstrating that Pb^{2+} adsorption on MOF nanosheets was primar-

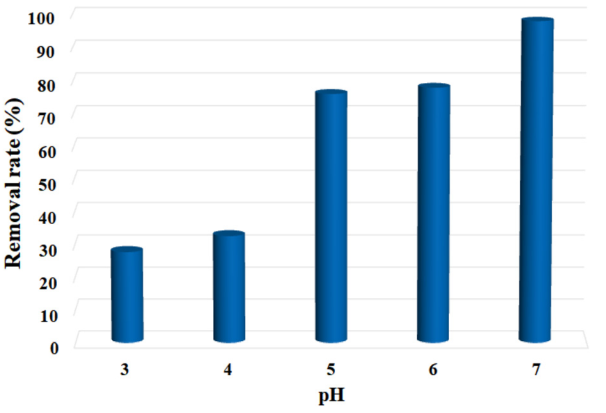

Fig. 3 pH effect on the removal efficiency of Pb^{2+} by MOF nanosheets. C_0 = 10 ppm, $m_{adsorbent}$ = 5 mg, V = 50 mL, pH = 3.0–7.0.

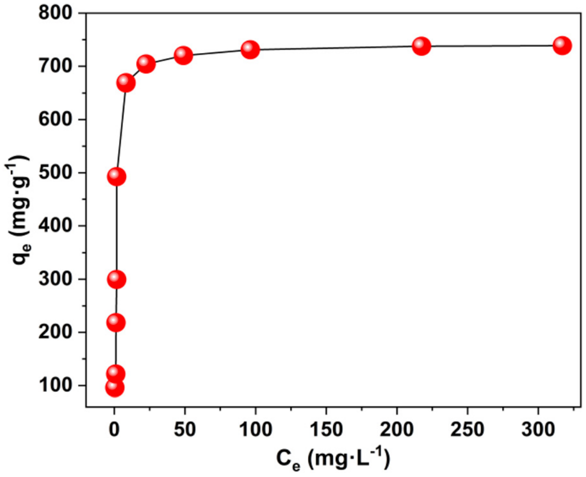

Fig. 4 Pb^{2+} adsorption isotherm for MOF nanosheets.

ily a monolayer adsorption behavior. The maximum uptake capacity was determined to be 746.26 mg g^{-1}. The estimated Pb^{2+} uptake capacity matched the experimental data well (738.65 mg g^{-1}), which was higher than that of the majority of Pb^{2+} adsorbents (Fig. 5 and Table S2†).

An adsorbent's reusability and stability are essential for the sustainable use of resources. To examine the repeatability of MOF nanosheets, the Pb^{2+}-loaded samples were submerged in 0.1 mmol L^{-1} HNO_3 for desorption. The cycle performance shown in Fig. S8† demonstrates that MOF nanosheets hold a good regeneration ability. The Pb^{2+} removal rate decreased slightly with the increase in cycle number, and it could hold a removal rate of more than 84% even after five cycles. The minor reduction in Pb^{2+} adsorption capacity may be caused by the combined factors including insufficient desorption, trace amounts of the adsorbent loss and sample degradation. Moreover, the PXRD patterns of the regenerated MOF nanosheets matched those of the 2D MOF nanosheets (Fig. S9†), which are completely different from those of the calix[4]arene pro-ligand, confirming the stability of the 2D adsorbents. The stability was further supported by the FT-IR analysis, in which no obvious spectral change was observed after adsorbent regeneration (Fig. 8). These results revealed that the 2D MOF nanosheet retained its framework structure after the adsorption–desorption cycles.

For an adsorbent, poor selectivity would not only result in the binding of advantageous light elements, lowering their levels in the water, but also foul adsorbents, limiting their capacities to remove target pollutants. Thus, high selectivity is crucial for the practical use of an adsorbent, and it is of great necessity to explore the selective adsorption performance of **Cu-MOF** nanosheets. The adsorbents were added into aqueous solutions with different single metal ions (10 ppm) of Pb^{2+}, Na^+, K^+, Ca^{2+}, Mg^{2+}, Sr^{2+}, Co^{2+}, Ni^{2+}, Cd^{2+}, and Ba^{2+}, respectively. After reaching adsorption equilibrium, the removal efficiency for each ion was assessed. The result shown in Fig. 6

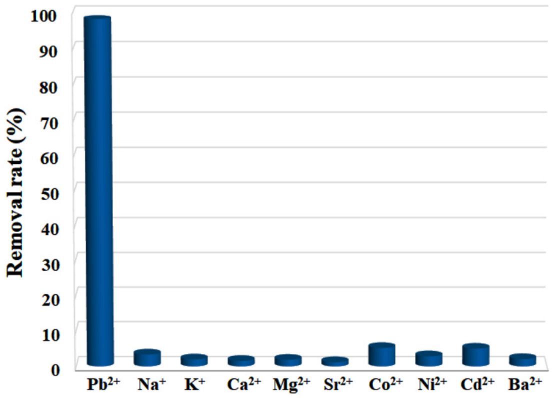

Fig. 6 Selective adsorption of MOF nanosheets for different metal ions.

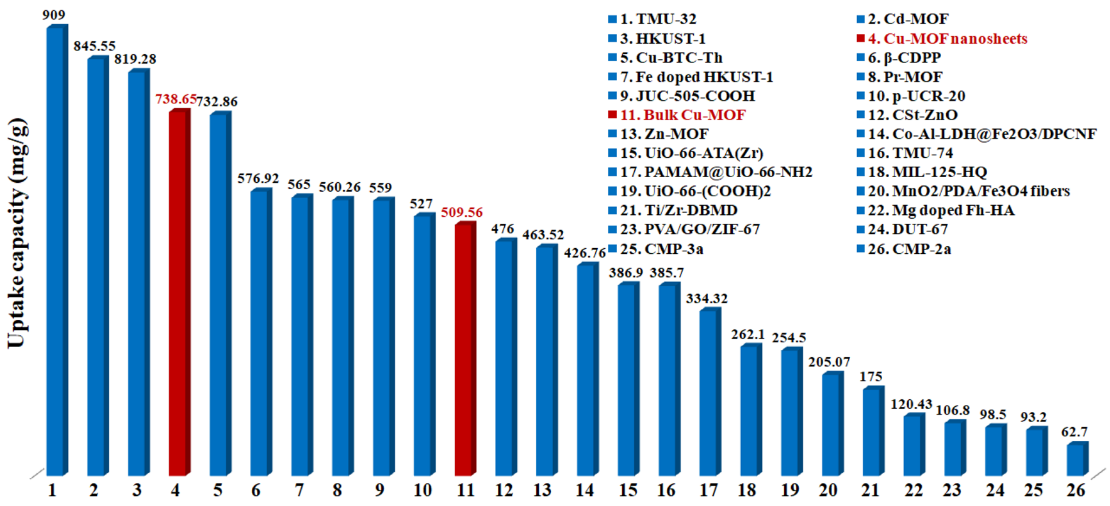

Fig. 5 Comparison of the maximum Pb^{2+} adsorption capacity for MOF nanosheets (no. 4) and bulk **Cu-MOFs** (no. 11) with various adsorbents (Table S2†).

demonstrates that Pb^{2+} has a substantially higher removal efficiency than that of other ions under the same condition. The removal efficiency for Pb^{2+} was 98.11%, while for other metal ions, the removal efficiencies were less than 5.08%. Thus, **Cu-MOF** nanosheets hold high selectivity for Pb^{2+}.

Coexisting ions are ubiquitous in aquatic systems, which might pose an effect on Pb^{2+} removal. It is highly desirable to assess the anti-interference performance of MOF nanosheets. The 2D nanosheets were added into a mixed solution containing Pb^{2+}, Na^+, K^+, Ca^{2+}, Mg^{2+}, Sr^{2+}, Co^{2+}, Ni^{2+}, Cd^{2+}, and Ba^{2+}, with a concentration of 10 ppm for each ion. After reaching adsorption equilibrium, 97.47% of Pb^{2+} was removed from the mixture (Table 1). The distribution coefficient K_d (mL g^{-1}) was calculated to assess the MOF nanosheets' affinities for Pb^{2+} in the presence of mixed ions,[46] and the K_d value was calculated to be 3.84×10^5 mL g^{-1} (Table 1). By comparison with the K_d value for Pb^{2+} in a solution (10 ppm) without any competing ions (5.20×10^5 mL g^{-1}), an ultra-high anti-interference ability toward interfering ions was obtained for **Cu-MOF** nanosheets. In daily life, the concentrations of some coexisting ions such as Ca^{2+}, Mg^{2+}, Na^+, and K^+ in drinking water were significantly higher than that of Pb^{2+}, thus it is imperative to explore Pb^{2+} adsorption behavior in the presence of other excess metal ions. The metal ions including Na^+, K^+, Ca^{2+}, Mg^{2+}, Sr^{2+}, Co^{2+}, Ni^{2+}, Cd^{2+}, and Ba^{2+} at a concentration of 50 ppm were separately added into the certain Pb^{2+} solution (10 ppm). After achieving adsorption balance, the Pb^{2+} removal performances were evaluated, respectively. As shown in Fig. 7, with high concentrations of different competing ions, the removal efficiencies for Pb^{2+} were no less than 88.17%. Encouraged by the good anti-interference performance of MOF nanosheets, the Pb^{2+} (10 ppm) removal performance was further evaluated in the presence of highly concentrated mixed ions. As presented in Table 1, even in the presence of 50 ppm (five times) of mixed competing ions, the removal ratio for Pb^{2+} can reach up to 86.71%, together with an excellent K_d value.

The above-mentioned results of selectivity and anti-interference experiments indicated the strong affinity of **Cu-MOF** nanosheets toward Pb^{2+} and ultrahigh anti-interference ability toward interfering ions, which can be ascribed to the following reasons. On the one hand, the numerous carboxyl and ether groups decorated on MOF nanosheets have the characteristics of a borderline base, making it easy to interact with the borderline acids of Co^{2+}, Ni^{2+}, and Pb^{2+}, and soft acid of Cd^{2+} but challenging with the hard acids of Na^+, K^+, Ca^{2+}, Mg^{2+}, Sr^{2+}, and Ba^{2+}.[43] The obtained low removal performance for Co^{2+}, Ni^{2+}, and Cd^{2+} shown in Fig. 6 could be attributed to their much higher hydration energies (1915 kJ mol^{-1} for Co^{2+}, 1980 kJ mol^{-1} for Ni^{2+}, and 1755 kJ mol^{-1} for Cd^{2+}) as compared to the obviously lower hydration energy for Pb^{2+} (1425 kJ mol^{-1}).[47] On the other hand, the larger ionic radius of Pb^{2+} (0.119 nm for Pb^{2+}, 0.069 nm for Ni^{2+}, 0.075 nm for Co^{2+}, and 0.095 nm for Cd^{2+}) could be allowed for more convenient interaction with the functional groups on the adsorbents.[48] Moreover, the close contact and sufficient interactions on the exposed surface area would well enhance the adsorption selectivity of the **Cu-MOF** nanosheets, affording ultrahigh selectivity.

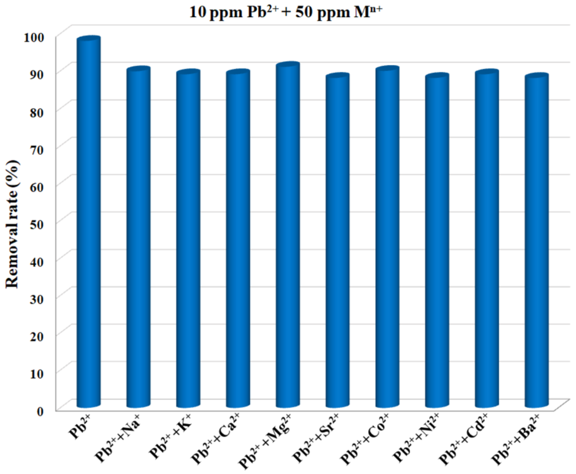

Fig. 7 Effect of the coexistent ions (50 ppm) on Pb^{2+} (10 ppm) removal by MOF nanosheets.

Table 1 Selective adsorption parameters of MOF nanosheets toward Pb^{2+}

Metal ions	C_0 (ppm)	Pb^{2+} removal rate (%)	K_d (mL g^{-1})
Pb^{2+}/M^{n+}	10/0	98.11	5.20×10^5
Pb^{2+}/M^{n+}	10/10	97.47	3.84×10^5
Pb^{2+}/M^{n+}	10/50	86.71	6.52×10^4

M^{n+} represent the mixed competition ions of Na^+, K^+, Ca^{2+}, Mg^{2+}, Sr^{2+}, Co^{2+}, Ni^{2+}, Cd^{2+}, and Ba^{2+}

Mechanism studies

To further understand the selective adsorption behavior of **Cu-MOF** nanosheets, the possible adsorption mechanism was investigated by a combination of techniques including zeta potential, FT-IR spectroscopy, and X-ray photoelectron spectroscopy (XPS). After Pb^{2+} adsorption, the zeta potential of the nanosheets changed from −31.88 mV to −4.95 mV (Fig. S10†), which is direct evidence for electrostatic adsorption. To further corroborate the electrostatic interaction in Pb^{2+} adsorption, the zeta potential of MOF nanosheets was examined at various pH levels. As shown in Fig. S11a,† the potential of MOF nanosheets rapidly declined as the solution pH increased. The result is understandable since the adsorption sites were protonated and covered with H^+ at lower pH, affording higher potentials; when the solution pH increased, the deprotonation of the adsorbents led to a lower potential for the MOF nanosheets. Nevertheless, the removal rate of Pb^{2+} followed an opposite trend, increasing dramatically as the solution pH rose (Fig. S11b†). Thus, the lower potential is beneficial for positively charged Pb^{2+} adsorption. The above-mentioned results indicated that the electrostatic interaction played a crucial role in Pb^{2+} adsorption. While at pH = 3.0, the MOF nanosheets exhibited a removal rate of 27.94% for Pb^{2+} (Fig. S11b†), which revealed the presence of other interactions in Pb^{2+} adsorption.

Then, a new question arose: what force, besides electrostatic attraction, is responsible for Pb^{2+} adsorption? For the answer, measurements of FT-IR and XPS spectra were conducted. In Fig. 8b, a new peak appeared at 509 cm^{-1} after Pb^{2+} adsorption, assigned to the stretching vibration of the Pb–O bond, which vanished after Pb^{2+} desorption, providing direct evidence for the coordination interactions between Pb^{2+} and O atoms. The peak shifts of the asymmetric and symmetric vibration of the aromatic ethers (=C–O–C–), from 1200 and 1051 cm^{-1} to 1192 and 1034 cm^{-1} after Pb^{2+} adsorption, proved the interactions between Pb^{2+} and ether groups. Moreover, the peaks at 3362, 1588, and 1340 cm^{-1} are attributed to the carboxyl (–COOH) vibration in MOF nanosheets, which shifted to 3393, 1583, and 1331 cm^{-1} after Pb^{2+} adsorption, demonstrating the coordination between carboxyl groups and Pb^{2+}.

The interactions between MOF nanosheets and Pb^{2+} were further investigated by XPS studies. The new peaks of Pb 4f, Pb 4d, and Pb 4p that emerged following Pb^{2+} adsorption provided more evidence for Pb^{2+} adsorption onto MOF nanosheets (Fig. S12a†). The high-resolution XPS of Pb 4f gave detailed information on Pb species. As shown in Fig. S12b,† two peaks centered at 143.3 eV and 138.4 eV were attributed to Pb $4f_{5/2}$ and Pb $4f_{7/2}$, which showed a remarkable shift of 1.0 eV to a lower binding energy, by comparison with Pb^{2+} binding energies of purified $Pb(NO_3)_2$ located at 144.5 eV (Pb $4f_{5/2}$) and 139.6 eV (Pb $4f_{7/2}$).[49] The notable peak shift demonstrated a strong affinity between Pb^{2+} and MOF nanosheets.[50] The energy separation of 4.9 eV between the peaks of Pb $4f_{5/2}$ (143.5 eV) and Pb $4f_{7/2}$ (138.6 eV) further supported the notion that coordination interaction, not merely the electrostatic contact, accounted for Pb^{2+} adsorption.[51,52] These findings are coincident with zeta potential studies and FT-IR analysis, and the strong electrostatic attractions and coordination interactions between Pb^{2+} and the carboxyl/ether groups are the key factors affecting Pb^{2+} adsorption.

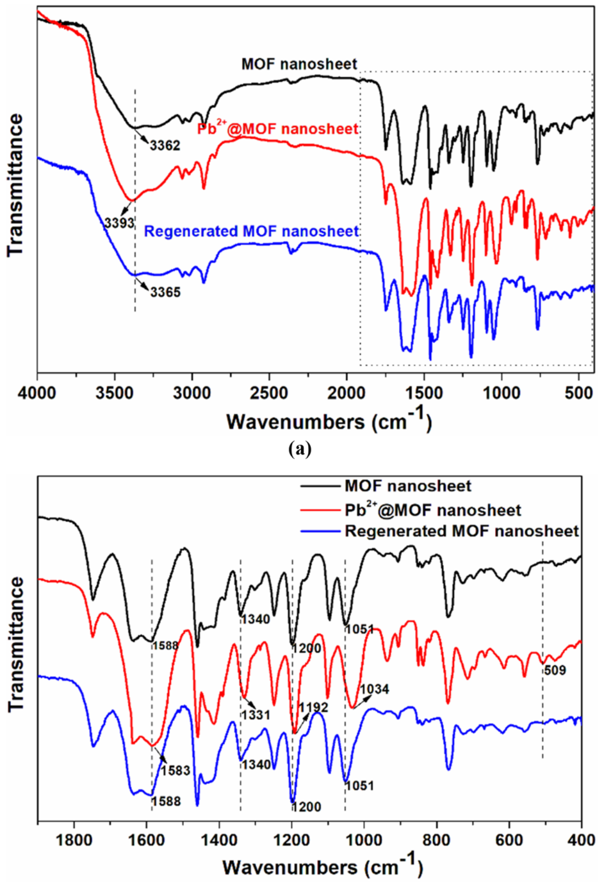

(a)

(b)

Fig. 8 Comparison of the FT-IR spectra at 400–4000 cm^{-1} (a) and 400–1900 cm^{-1} (b) for MOF nanosheets, Pb^{2+}@MOF nanosheets, and regenerated MOF nanosheets.

The density functional theory (DFT) calculation was further introduced for the investigation of the adsorption mechanism between the adsorbent and Pb^{2+} at the molecular level. Due to the time-consuming nature of the DFT calculation, the structural unit of the cage-like cavity in **Cu-MOF** was selected as a representative theoretical model for calculation. Five models were constructed, in which Pb^{2+} was encapsulated in the cage-like cavities. The optimized coordinated geometries for the cage-like building unit, possible interactions, Gibbs free energy (ΔG), and interaction distances (Pb–O) are shown in Fig. 9. In model a, Pb^{2+} was interacted with four O atoms from four ether groups and one O atom from a deprotonated carboxyl group (Fig. 9a). Model b shows that Pb^{2+} was chelated by four O atoms from ether groups (Fig. 9b). The ΔG value of Model b (−145.48 kcal mol^{-1}) is more positive than that of model a (−149.23 kcal mol^{-1}), indicating that the interactions of Pb^{2+} with both carboxylate and ether groups in model a are more thermodynamically favorable. For other models (Fig. 9c–e), Pb^{2+} was chelated with one carboxylate group in Model c and two carboxylate groups in Model d, and bridged by two carboxylate groups in Model e, respectively. The ΔG values (−113.36 kcal mol^{-1} for Model c, −94.97 kcal mol^{-1} for Model d, and −74.94 kcal mol^{-1} for Model e) of these models are much positive than those of model a. These results illustrate that the combined action between carboxylate and ether groups with Pb^{2+} is more effective than the interactions of the independent ether or carboxylate group with Pb^{2+}, which is consistent with the FT-IR analysis. As a result, the carboxylate and ether groups in the cage-like cavity worked together to capture Pb^{2+}. In addition, the average distance of the Pb–O bond in model a (2.27 Å, Fig. 9) is obviously shorter than that in other models (2.69 Å for Model b, 2.70 Å for Model c, 2.63 Å for Model d and 2.77 Å for Model e), which further illustrates that the cooperative interaction of the carboxylate and ether groups has a stronger affinity for Pb^{2+}, leading to more efficient extraction of Pb^{2+}.

An essential factor in describing the adsorption behavior is the adsorption binding energy. Adsorption happens spontaneously indicated by a negative adsorption binding energy; otherwise, adsorption requires external energy.[53] The smaller

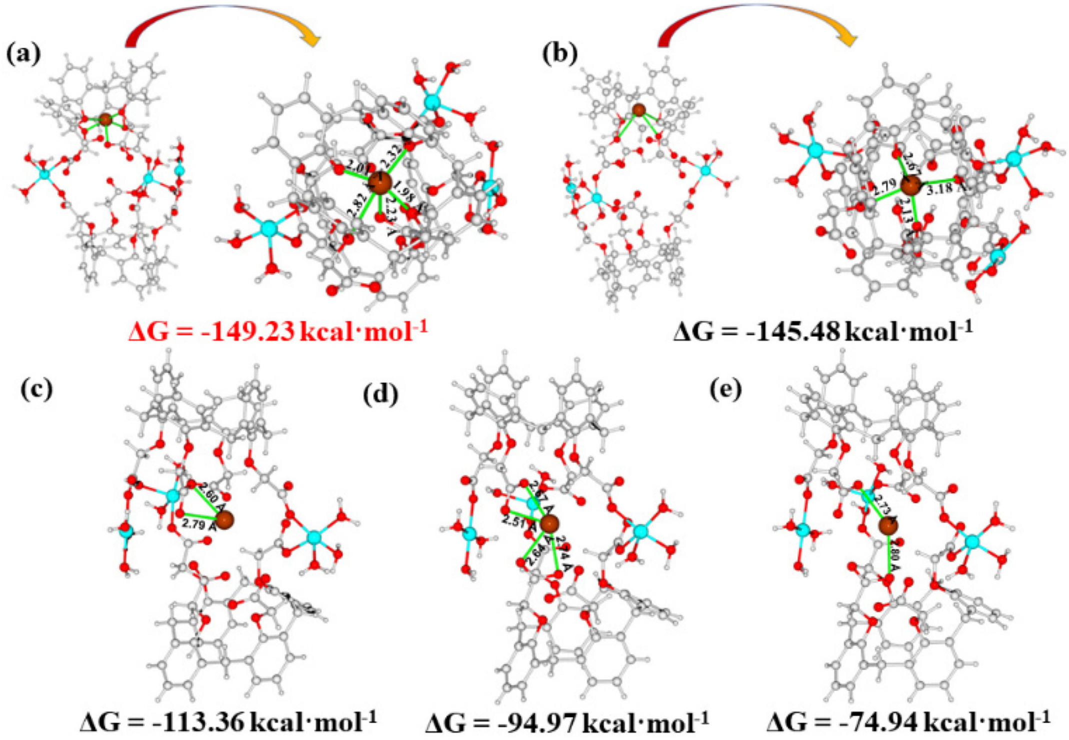

Fig. 9 (a–e) Optimized cage-like cavity in **Cu-MOFs** through DFT simulation and identification of the possible types of interactions with Pb^{2+} during the adsorption process. Color codes: cyan, Cu; brown, Pb; red, O; gray, C; light gray, H.

the value of the adsorption binding energy, the stronger the adsorption binding affinity.[54] The adsorption binding energies for Pb^{2+} and various metal ions such as Na^+, K^+, Ca^{2+}, Mg^{2+}, Sr^{2+}, Co^{2+}, Ni^{2+}, Cd^{2+}, and Ba^{2+}, were calculated with the aid of DFT calculations, to clarify the selective adsorption of **Cu-MOF** nanosheets. The resulting adsorption binding energies, interaction distances and the optimized equilibrium adsorption configurations are shown in Fig. 10. The adsorption binding energy for Pb^{2+} was negative, which revealed that Pb^{2+} adsorption on **Cu-MOF** nanosheets was a spontaneous behavior. The negative adsorption binding energy (−7.16 eV) of Pb^{2+} is significantly lower than that of other metal ions (Fig. 10), indicating that the cage-like cavity has an obviously higher affinity for Pb^{2+}, which is in good agreement with the result of ultra-high K_d values of Pb^{2+} shown in Table 1. Moreover, the obviously shorter interaction distance for the Pb–O bond shown in Fig. 10 further verifies the strong affinity for Pb^{2+}.

The above-mentioned results on the experimental and theoretical investigations demonstrated an ultrahigh adsorption selectivity of **Cu-MOF** nanosheets toward Pb^{2+}. As a comparison, the selective adsorption performance of 3D **Cu-MOF** was investigated. High selectivity can also be achieved for Pb^{2+} (Fig. S13†), while it is inferior to that of the MOF nanosheets. For the anti-interference ability of 3D **Cu-MOFs**, it is obviously lower than that of 2D **Cu-MOF** nanosheets (Fig. S14 and Table S3†). To better understand the lower selectivity and anti-interference ability for 3D **Cu-MOFs**, the measurements of zeta potential, FT-IR spectroscopy, and XPS were performed to investigate the possible adsorption mechanism. Similar results were obtained, which were presented in Fig. S15–S17 in the ESI,† followed by relevant analysis on the adsorption mechanism of 3D **Cu-MOFs**, revealing a similar adsorption mechanism to that of the 2D MOF nanosheets. Thus, 3D **Cu-MOFs** with the same framework structure, but different dimensions, as that of its 2D counterpart presented similar adsorption mechanisms but lower adsorption selectivity and anti-interference ability. This result is understandable. For these MOF adsorbents, the strong electrostatic attractions and coordination interactions are the key factors affecting Pb^{2+} adsorption. Specifically, before close contact with pollutant molecules, the adsorption driving force is electrostatic attraction, which showed low selectivity; while in close contact with pollutant molecules, the main interaction is the coordination interaction, that is, the adsorption binding energies dominated the adsorption process, which showed high selectivity. For the 2D MOF nanosheets, the exposed surface area provided the adsorption sites with more chance for close contact and sufficient interaction with pollutant molecules, which made the adsorption binding energies greatly contribute to the adsorption process, substantially enhancing the adsorption selectivity of the 2D MOF nanosheets. For the 3D MOF adsorbents, it is difficult for the buried adsorption sites in the frameworks to contact pollutant molecules closely, thus the adsorption driving force, electrostatic attraction, dominated the adsorption for most of the time. As a result, the insufficiently close contact results in lower adsorption selectivity for 3D **Cu-MOF**.

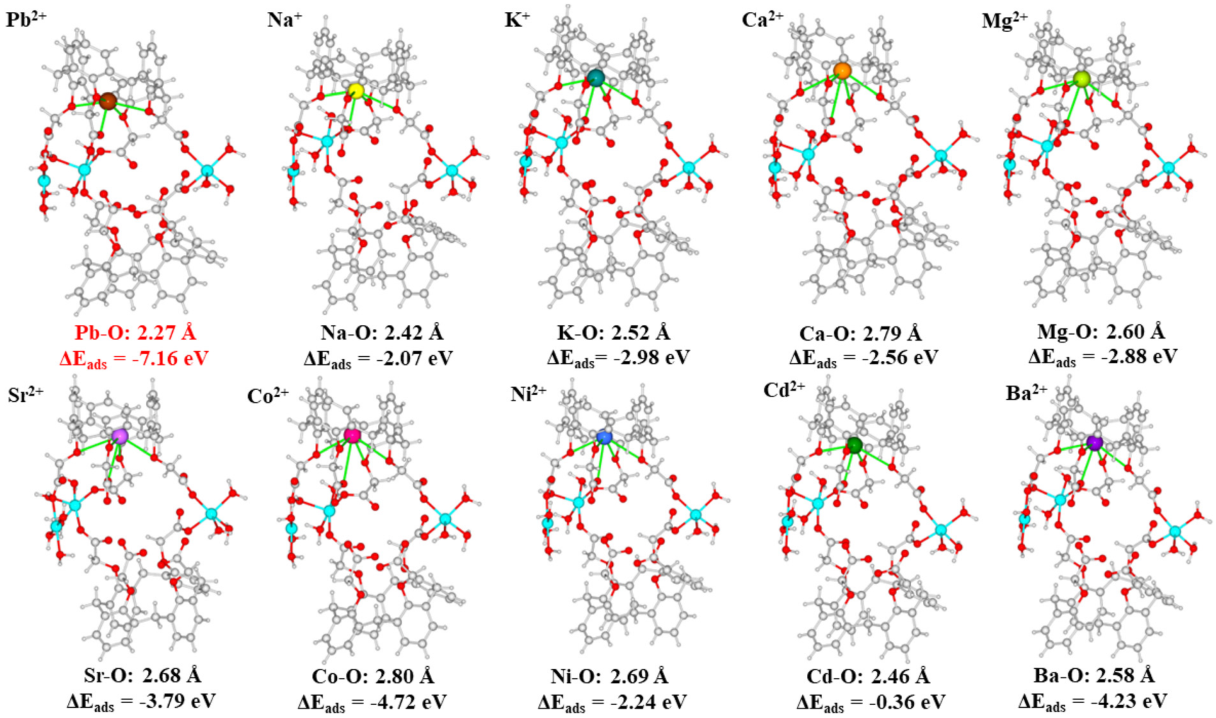

Fig. 10 DFT calculation models for metal ions of Pb^{2+}, Na^{+}, K^{+}, Mg^{2+}, Ca^{2+}, Sr^{2+}, Co^{2+}, Ni^{2+}, Cd^{2+}, and Ba^{2+}.

The adsorption isotherms were further investigated to estimate the maximum adsorption capacity of 3D **Cu-MOFs**. As expected, the limited access to the buried adsorption sites in the framework resulted in a lower Pb^{2+} adsorption capacity of 509.56 mg g^{-1} for 3D **Cu-MOF** (Fig. S18–S19†). These results revealed that well-improved Pb^{2+} adsorption performance can be achieved by MOF exfoliation. In contrast to 3D porous adsorbents, the 2D **Cu-MOF** nanosheets not only inherit the structural characteristics of MOFs, such as periodic structures with predesigned adsorption sites, but also overcome the drawbacks of 3D porous materials, such as restricted access to the active sites, which made the adsorption sites fully utilized, affording well-enhanced adsorption performance. Different from the conventional MOF nanosheets, **Cu-MOF** nanosheets were decorated with cavity structures that were beneficial for adsorption, there were predesigned adsorption sites (uncoordinated carboxyl and ether groups) decorated in the cativy structures. The exposed surface area of **Cu-MOF** nanosheets endowed the sites with accessibility for close contact and sufficient interactions with target pollutants, which greatly enhanced the adsorption selectivity and uptake capacity.

Conclusions

In conclusion, an ultrathin 2D MOF nanosheet with cage-like cavities has been built based on the calix[4]arene for the first time. The as-prepared ultrathin nanosheets, with a thickness of 5.8 ± 0.1 nm, showed extremely selective adsorption performance toward Pb^{2+}, even with the existence of highly concentrated competing ions. The adsorption capacity of Pb^{2+} can reach up to 738.65 mg g^{-1}, exceeding that of most adsorbents. The adsorption performances of 2D **Cu-MOF** nanosheets, including adsorption selectivity, anti-interference ability, and uptake capacity, are obviously better than those of 3D **Cu-MOFs**, which can be ascribed to the unique structure of the exposed surface area with cavity structures. The calix[4]arene, an ideal building block for the construction of 2D materials with cage-like cavities, not only facilitates the exfoliation of the 3D precursor but also provides the cavity structures and adsorption sites that are beneficial for adsorption. The intimate contact and sufficient interactions between the active sites in the cavities on the exposed surface areas with pollutant molecules could achieve highly efficient capture and ultra-high adsorption selectivity. Our work may provide a perspective for broadening the scope of functionalities on 2D materials in the future, and create many high-performance adsorbents.

Data availability

All experimental data is available in the ESI.†

Author contributions

L.-L. Liu and D. Liu conceived and directed the project. C.-X. Yu wrote the manuscript and analyzed the data. H. Sun and K.-Z. Wang performed the experiments and analyzed preliminary results. All the authors discussed the results and gave approval to the final version of the manuscript.

Conflicts of interest

There are no conflicts to declare.

Acknowledgements

This work was supported by the Natural Science Foundation of Shandong Province (ZR2021MB106 and ZR2021QB090), the Major Projects of Natural Science Research in Universities of Jiangsu Province (20KJA150002) and the Huaishang Talent Program of Huaian.

References

1 M. Ren, X. Qian, Y. Chen, T. Wang and Y. Zhao, Potential lead toxicity and leakage issues on lead halide perovskite photovoltaics, *J. Hazard. Mater.*, 2022, **426**, 127848.

2 A. R. Geisse, C. M. Ngule and D. T. Genna, Removal of lead ions from water using thiophene-functionalized metal-organic frameworks, *Chem. Commun.*, 2020, **56**, 237–240.

3 M. E. Mahmoud, M. F. Amira, S. M. Seleim and A. K. Mohamed, Amino-decorated magnetic metal-organic framework as a potential novel platform for selective removal of chromium(vI), cadmium(II) and lead(II), *J. Hazard. Mater.*, 2020, **381**, 120979.

4 J. Tang, Y. Chen, M. Zhao, S. Wang and L. Zhang, Phenylthiosemicarbazide-functionalized UiO-66-NH_2 as highly efficient adsorbent for the selective removal of lead from aqueous solutions, *J. Hazard. Mater.*, 2021, **413**, 125278.

5 D. Wu, P.-F. Zhang, G.-P. Yang, L. Hou, W.-Y. Zhang, Y.-F. Han, P. Liu and Y.-Y. Wang, Supramolecular control of MOF pore properties for the tailored guest adsorption/separation applications, *Coord. Chem. Rev.*, 2021, **434**, 213709.

6 S. Sharma, A. V. Desai, B. Joarder and S. K. Ghosh, A water-stable ionic MOF for the selective capture of toxic oxoanions of Se^{VI} and As^{V} and crystallographic insight into the ion-exchange mechanism, *Angew. Chem., Int. Ed.*, 2020, **59**, 7788–7792.

7 Z. Shao, J. Chen, K. Gao, Q. Xie, X. Xue, S. Zhou, C. Huang, L. Mi and H. Hou, A double-helix metal-chain metal-organic framework as a high-output triboelectric nanogenerator material for self-powered anticorrosion, *Angew. Chem., Int. Ed.*, 2022, **61**, e202208994.

8 J. Liu, J. Xue, G.-P. Yang, L.-L. Dang, L.-F. Ma, D.-S. Li and Y.-Y. Wang, Recent advances of functional heterometallic-organic framework (HMOF) materials: Design strategies and applications, *Coord. Chem. Rev.*, 2022, **463**, 214521.

9 J. Guo, Y. Qin, Y. Zhu, X. Zhang, C. Long, M. Zhao and Z. Tang, Metal-organic frameworks as catalytic selectivity regulators for organic transformations, *Chem. Soc. Rev.*, 2021, **50**, 5366–5396.

10 S. A. A. Razavi and A. Morsali, Linker functionalized metal-organic frameworks, *Coord. Chem. Rev.*, 2019, **399**, 213023.

11 R. Zhao, T. Ma, S. Zhao, H. Rong, Y. Tian and G. Zhu, Uniform and stable immobilization of metal-organic frameworks into chitosan matrix for enhanced tetracycline removal from water, *Chem. Eng. J.*, 2020, **382**, 122893.

12 F. Afshariazar, A. Morsali, J. Wang and P. C. Junk, Highest and fastest removal rate of Pb^{II} ions through rational functionalized decoration of a metal-organic framework cavity, *Chem. – Eur. J.*, 2020, **26**, 1355–1362.

13 Y. Cui, Z. Shao, Y. Zhao, K. Geng, T. Wen, J. Wu and H. Hou, Thermal steam reduction etching to construct POM@$Cu^{I}Cu^{II}$-BTC with hierarchical porosity for adsorption property enhancement, *Chem. Eng. J.*, 2022, **450**, 137966.

14 A. H. Vahabi, F. Norouzi, E. Sheibani and M. Rahimi-Nasrabadi, Functionalized Zr-UiO-67 metal-organic frameworks: Structural landscape and application, *Coord. Chem. Rev.*, 2021, **445**, 214050.

15 L. Pei, X. Zhao, B. Liu, Z. Li and Y. Wei, Rationally tailoring pore and surface properties of metal-organic frameworks for boosting adsorption of Dy^{3+}, *ACS Appl. Mater. Interfaces*, 2021, **13**, 46763–46771.

16 R.-D. Wang, L. He, R.-R. Zhu, M. Jia, S. Zhou, J. Tang, W.-Q. Zhang, L. Du and Q.-H. Zhao, Highly efficient and selective capture Pb(II) through a novel metal-organic framework containing bifunctional groups, *J. Hazard. Mater.*, 2022, **427**, 127852.

17 J. Su, M. Yuan, L. Han, H. Deng, J. Chang, Y. Zhuang, J. Wang and Y. Zhang, Ultrathin metal organic framework nanosheets with rich defects for enhanced fluoride removal, *Chem. Eng. J.*, 2023, **451**, 138989.

18 M. Wang, R. Dong and X. Feng, Two-dimensional conjugated metal-organic frameworks (2D c-MOFs): chemistry and function for MOF tronics, *Chem. Soc. Rev.*, 2021, **50**, 2764–2793.

19 M. Abbas, A. M. Maceda, H. R. Firouzi, Z. Xiao, H. D. Arman, Y. Shi, H.-C. Zhou and K. J. Balkus, Fluorine extraction from organofluorine molecules to make fluorinated clusters in yttrium MOFs, *Chem. Sci.*, 2022, **13**, 14285–14291.

20 H. An, Y. Hu, N. Song, T. Mu, S. Bai, Y. Peng, L. Liu and Y. Tang, Two-dimensional heterostructures built from ultrathin CeO_2 nanosheet surface-coordinated and confined metal-organic frameworks with enhanced stability and catalytic performance, *Chem. Sci.*, 2022, **13**, 3035–3044.

21 L.-L. Liu, J. Chen, Y. Zhang, C.-X. Yu, W. Du, X.-Q. Sun, J.-L. Zhang, F.-L. Hu, Y. Mi and L.-F. Ma, Fabrication of ultrathin single-layer 2D metal-organic framework nanosheets with excellent adsorption performance via a facile exfoliation approach, *J. Mater. Chem. A*, 2021, **9**, 546–555.

22 B. Garai, D. Shetty, T. Skorjanc, F. Gándara, N. Naleem, S. Varghese, S. K. Sharma, M. Baias, R. Jagannathan, M. A. Olson, S. Kirmizialtin and A. Trabolsi, Taming the

topology of calix[4]arene-based 2D-covalent organic frameworks: Interpenetrated vs noninterpenetrated frameworks and their selective removal of cationic dyes, *J. Am. Chem. Soc.*, 2021, **143**, 3407–3415.

23 G. A. Bhat, S. Haldar, S. Verma, D. Chakraborty, R. Vaidhyanathan and R. Murugavel, Facile exfoliation of single-crystalline copper alkylphosphates to single-layer nanosheets and enhanced supercapacitance, *Angew. Chem., Int. Ed.*, 2019, **58**, 16844–16849.

24 Y. Cheng, S. J. Datta, S. Zhou, J. Jia, O. Shekhah and M. Eddaoudi, Advances in metal-organic framework-based membranes, *Chem. Soc. Rev.*, 2022, **51**, 8300–8350.

25 C.-X. Yu, X.-J. Li, J.-S. Zong, D.-J. You, A.-P. Liang, Y.-L. Zhou, X.-Q. Li and L.-L. Liu, Fabrication of protonated two-dimensional metal-organic framework nanosheets for highly efficient iodine capture from water, *Inorg. Chem.*, 2022, **61**, 13883–13892.

26 J. Guo, X. Xue, H. Yu, Y. Duan, F. Li, Y. Lian, Y. Liu and M. Zhao, Metal-organic frameworks based on infinite secondary building units: recent progress and future outlooks, *J. Mater. Chem. A*, 2022, **10**, 19320–19347.

27 W.-Q. Tang, Y.-J. Zhao, M. Xu, J.-Y. Xu, S.-S. Meng, Y.-D. Yin, Q.-H. Zhang, L. Gu, D.-H. Liu and Z.-Y. Gu, Controlling the stacking modes of metal-organic framework nanosheets through host-guest noncovalent interactions, *Angew. Chem., Int. Ed.*, 2021, **60**, 6920–6925.

28 Q. Zhang, P.-S. Cao, Y. Cheng, S.-S. Yang, Y.-D. Yin, T.-Y. Lv and Z.-Y. Gu, Nonlinear ion transport through ultrathin metal-organic framework nanosheet, *Adv. Funct. Mater.*, 2020, **30**, 2004854.

29 Q. Deng, X. Hou, Y. Zhong, J. Zhu, J. Wang, J. Cai, Z. Zeng, J.-J. Zou, S. Deng, T. Yoskamtorn and S. C. E. Tsang, 2D MOF with compact catalytic sites for the one-pot synthesis of 2,5-dimethylfuran from saccharides via tandem catalysis, *Angew. Chem., Int. Ed.*, 2022, **61**, e202205453.

30 C.-X. Yu, W. Jiang, K.-Z. Wang, A.-P. Liang, J.-G. Song, Y.-L. Zhou, X.-Q. Sun and L.-L. Liu, Luminescent two-dimensional metal-organic framework nanosheets with large π-conjugated system: Design, synthesis, and detection of anti-inflammatory drugs and pesticides, *Inorg. Chem.*, 2022, **61**, 982–991.

31 Y. Qin, Z. Li, Y. Duan, J. Guo, M. Zhao and Z. Tang, Nanostructural engineering of metal-organic frameworks: Construction strategies and catalytic applications, *Matter*, 2022, **5**, 3260–3310.

32 Z. Wang, G. Wang, H. Qi, M. Wang, M. Wang, S. Park, H. Wang, M. Yu, U. Kaiser, A. Fery, S. Zhou, R. Dong and X. Feng, Ultrathin two-dimensional conjugated metal-organic framework single-crystalline nanosheets enabled by surfactant-assisted synthesis, *Chem. Sci.*, 2020, **11**, 7665–7671.

33 M. Zhao, Y. Huang, Y. Peng, Z. Huang, Q. Ma and H. Zhang, Two-dimensional metal-organic framework nanosheets: synthesis and applications, *Chem. Soc. Rev.*, 2018, **47**, 6267–6295.

34 J. Li, Q. Duan, Z. Wu, X. Li, K. Chen, G. Song, A. Alsaedi, T. Hayat and C. Chen, Few-layered metal-organic framework nanosheets as a highly selective and efficient scavenger for heavy metal pollution treatment, *Chem. Eng. J.*, 2020, **383**, 123189.

35 Y. Qin, Y. Wan, J. Guo and M. Zhao, Two-dimensional metal-organic framework nanosheet composites: Preparations and applications, *Chin. Chem. Lett.*, 2022, **33**, 693–702.

36 R. Xu, M. Jian, Q. Ji, C. Hu, C. Tang, R. Liu, X. Zhang and J. Qu, 2D water-stable zinc-benzimidazole framework nanosheets for ultrafast and selective removal of heavy metals, *Chem. Eng. J.*, 2020, **382**, 122658.

37 T. Skorjanc, D. Shetty, F. Gándara, S. Pascal, N. Naleem, S. Abubakar, L. Ali, A. K. Mohammed, J. Raya, S. Kirmizialtin, O. Siri and A. Trabolsi, Covalent organic framework based on azacalix[4]arene for the efficient capture of dialysis waste products, *ACS Appl. Mater. Interfaces*, 2022, **14**, 39293–39298.

38 Y.-X. Ma, B. Gao, Y. Li, W. Wei, Y. Zhao and J.-F. Ma, Macrocycle-based metal-organic frameworks with NO_2-driven on/off switch of conductivity, *ACS Appl. Mater. Interfaces*, 2021, **13**, 27066–27073.

39 H.-Y. Tong, J. Liang, Q.-J. Wu, Y.-H. Zou, Y.-B. Huang and R. Cao, Soluble imidazolium-functionalized coordination cages for efficient homogeneous catalysis of CO_2 cycloaddition reactions, *Chem. Commun.*, 2021, **57**, 2140–2143.

40 F.-F. Wang, C. Liu, J. Yang, H.-L. Xu, W.-Y. Pei and J.-F. Ma, A sulfur-containing capsule-based metal-organic electrochemical sensor for super-sensitive capture and detection of multiple heavy-metal ions, *Chem. Eng. J.*, 2022, **438**, 135639.

41 C.-X. Yu, F.-L. Hu, J.-G. Song, J.-L. Zhang, S.-S. Liu, B.-X. Wang, H. Meng, L.-L. Liu and L.-F. Ma, Ultrathin two-dimensional metal-organic framework nanosheets decorated with tetra-pyridyl calix[4]arene: Design, synthesis and application in pesticide detection, *Sens. Actuators, B*, 2020, **310**, 127819.

42 C. Tan, K. Yang, J. Dong, Y. Liu, Y. Liu, J. Jiang and Y. Cui, Boosting enantioselectivity of chiral organocatalysts with ultrathin two-dimensional metal-organic framework nanosheets, *J. Am. Chem. Soc.*, 2019, **141**, 17685–17695.

43 R. G. Pearson, Hard and soft acids and bases, *J. Am. Chem. Soc.*, 1963, **85**, 3533–3539.

44 Y. Jiang, L. Cao, X. Hu, Z. Ren, C. Zhang and C. Wang, Simulating powder X-ray diffraction patterns of two-dimensional materials, *Inorg. Chem.*, 2018, **57**, 15123–15132.

45 Y.-H. Luo, C. Chen, C. He, Y.-Y. Zhu, D.-L. Hong, X.-T. He, P.-J. An, H.-S. Wu and B.-W. Sun, Single-layered two-dimensional metal-organic framework nanosheets as an in situ visual test paper for solvents, *ACS Appl. Mater. Interfaces*, 2018, **10**, 28860–28867.

46 C. Yu, Z. Shao and H. Hou, A functionalized metal-organic framework decorated with O^- groups showing excellent performance for lead(II) removal from aqueous solution, *Chem. Sci.*, 2017, **8**, 7611–7619.

47 Y. Marcus, Thermodynamics of solvation of ions. Part 5.-Gibbs free energy of hydration at 298.15 K, *J. Chem. Soc., Faraday Trans.*, 1991, **87**, 2995–2999.

48 X. Yu, S. Tong, M. Ge, L. Wu, J. Zuo, C. Cao and W. Song, Adsorption of heavy metal ions from aqueous solution by carboxylated cellulose nanocrystals, *J. Environ. Sci.*, 2013, **25**, 933–943.

49 Q. Peng, J. Guo, Q. Zhang, J. Xiang, B. Liu, A. Zhou, R. Liu and Y. Tian, Unique lead adsorption behavior of activated hydroxyl group in two-dimensional titanium carbide, *J. Am. Chem. Soc.*, 2014, **136**, 4113–4116.

50 J. Wang, W. Zhang, X. Yue, Q. Yang, F. Liu, Y. Wang, D. Zhang, Z. Li and J. Wang, One-pot synthesis of multifunctional magnetic ferrite-MoS_2-carbon dot nanohybrid adsorbent for efficient Pb(II) removal, *J. Mater. Chem. A*, 2016, **4**, 3893–3900.

51 D. Chen, W. Shen, S. Wu, C. Chen, X. Luo and L. Guo, Ion exchange induced removal of Pb(II) by MOF-derived magnetic inorganic sorbents, *Nanoscale*, 2016, **8**, 7172–7179.

52 L. J. Chen, S. M. Zhang, Z. S. Wu, Z. J. Zhang and H. X. Dang, Preparation of PbS-type PbO nanocrystals in a room-temperature ionic liquid, *Mater. Lett.*, 2005, **59**, 3119–3121.

53 F. Calle-Vallejo, D. Loffreda, M. T. M. Koper and P. Sautet, Introducing structural sensitivity into adsorption-energy scaling relations by means of coordination numbers, *Nat. Chem.*, 2015, **7**, 403–410.

54 L. Zheng, S. Zhang, W. Cheng, L. Zhang, P. Meng, T. Zhang, H. Yu and D. Peng, Theoretical calculations, molecular dynamics simulations and experimental investigation of the adsorption of cadmium(II) on amidoxime-chelating cellulose, *J. Mater. Chem. A*, 2019, **7**, 13714–13726.